

Performance and characteristics of the BILBY time-of-flight small-angle neutron scattering instrument

Anna Sokolova,* Andrew E. Whitten,* Liliana de Campo,* Jason Christoforidis, Andrew Eltobaji, John Barnes, Frank Darmann and Andrew Berry

Australian Centre for Neutron Scattering, Australian Nuclear Science and Technology Organisation, New Illawarra Road, Lucas Heights, NSW 2234, Australia. *Correspondence e-mail: anna.sokolova@ansto.gov.au, andrew.whitten@ansto.gov.au, liliana.decampo@ansto.gov.au

Received 8 March 2018

Accepted 20 December 2018

Edited by E. P. Gilbert, ANSTO, Kirrawee DC, Australia

Keywords: small-angle neutron scattering; time-of-flight instruments; instrumentation; high resolution; nanostructures.

BILBY is a recently constructed and commissioned time-of-flight small-angle neutron scattering instrument, operated by the Australian Centre for Neutron Scattering at the Australian Nuclear Science and Technology Organisation (ANSTO). BILBY provides a wide accessible q range ($q \simeq 1.0 \times 10^{-3} \text{ \AA}^{-1}$ to $\sim 1.8 \text{ \AA}^{-1}$) and variable wavelength resolution ($\Delta\lambda/\lambda \simeq 3\text{--}30\%$) to complement the other small-angle and ultra-small-angle neutron scattering capabilities available at ANSTO. Since its construction, BILBY has been used to study samples from a wide range of scientific disciplines, including biology, chemistry, physics and materials science. This article describes the BILBY design and components, and shows data collected from a number of reference samples.

1. Introduction

Small-angle neutron scattering (SANS) is a well established and powerful technique used to study the nanostructure of various materials in the size range of 1–1000 nm. The Australian Centre for Neutron Scattering (ACNS), located at the Australian Nuclear Science and Technology Organisation (ANSTO), currently operates three SANS instruments: QUOKKA (Gilbert *et al.*, 2006; Wood *et al.*, 2018), a monochromatic SANS instrument with a q_{\min} of either $\sim 7.0 \times 10^{-4} \text{ \AA}^{-1}$ (with focusing optics) or $\sim 4.0 \times 10^{-3} \text{ \AA}^{-1}$ (without focusing optics) and $q_{\max} \simeq 1.5 \text{ \AA}^{-1}$; KOOKABURRA (Rehm *et al.*, 2013, 2018), a Bonse–Hart ultra-small-angle neutron scattering (USANS) instrument, with an accessible q range of between $\sim 1.8 \times 10^{-5}$ and 0.03 \AA^{-1} ; and BILBY, the new time-of-flight (ToF) instrument, with an accessible q range between $\sim 1.0 \times 10^{-3}$ and $\sim 1.8 \text{ \AA}^{-1}$, which is described herein.

The instrument characteristics for BILBY were settled upon during an international workshop held in August 2009, where it was decided that BILBY should provide a wide dynamic q range and variable wavelength resolution to complement the small-angle and ultra-small-angle neutron scattering capabilities available at ANSTO at that time. Access to a wide q range in a single measurement was deemed important for experiments where the evolution of a sample over time is investigated (*i.e.* the study of sample kinetics), while variable wavelength resolution caters for experiments where high wavelength resolution is required (such as resolving closely spaced diffraction peaks) and those where a higher neutron flux (and lower wavelength resolution) is preferable. On the basis of these criteria, it was decided that a ToF instrument would be the most appropriate choice. The

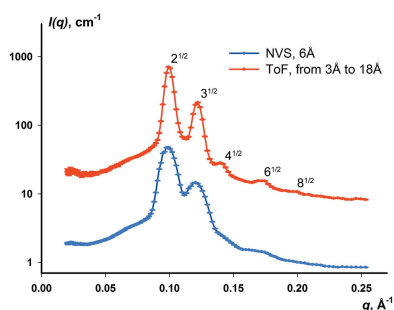




Figure 1 An overview of the BILBY instrument. (a) The neutron guide, which starts at the reactor wall, and connecting choppers marked 1, 2, 3 and 4. For reference, the distance between choppers 1 and 2 is 4.4 m. (b) The ~17 m long collimator, (c) the sample area and (d) the 19 m long detector tank.

design and construction project commenced in 2009 and was completed in 2015, and BILBY entered the ANSTO user programme in 2016.

The use of ToF SANS has its origins at the fast IBR-30 pulsed reactor at Dubna (Kuklin *et al.*, 2012) and at pulsed spallation neutron facilities (Ishikawa *et al.*, 1986; Seeger & Hjelm, 1991; Heenan *et al.*, 1997, 2011; Carpenter & Faber, 1978; Mildner, 1978), although its application at reactor-based sources is far more recent (Kampmann *et al.*, 2006; Dewhurst *et al.*, 2016). The primary advantage of using a ToF instrument over a conventional monochromatic instrument is that the ToF instrument allows access to a large q range in a specific configuration and allows, for example, kinetic experiments to be carried out without the need to stitch together data from different configurations and different samples. An additional advantage of using ToF on a reactor source is the ability to tune the pulse frequency and wavelength resolution to suit the experimental requirements, which cannot be achieved at a fixed-frequency spallation neutron source.

2. The BILBY instrument

2.1. Overview

BILBY is an ~40 m long SANS instrument with a maximum collimation length of ~17 m and a maximum sample-to-detector distance (SDD) of ~21 m. The design is based on the D33 instrument located at the Institut Laue–Langevin (ILL, Grenoble, France) (Dewhurst *et al.*, 2016), optimized to the characteristics of the 20 MW OPAL reactor and liquid-deuterium cold source. In the ToF mode, the neutron choppers create a pulsed neutron beam with a wavelength range between 2 and 20 Å. This neutron spectrum is comparable to that used by ToF SANS instruments at pulsed spallation neutron facilities (Ishikawa *et al.*, 1986; Seeger & Hjelm, 1991; Heenan *et al.*, 1997, 2011). Starting from the neutron guide that transports neutrons from the reactor to the choppers, the instrument is composed of four main sections: the neutron filters, comprising the neutron choppers, velocity selector, cut-off mirror, roughing slits and attenuators [Fig. 1, labelled (a)]; the collimator, comprising a set of precise slits, and translatable tables with reflecting neutron guides and boron-lined neutron-absorbing tubes with beam-defining apertures [Fig. 1, (b)]; the sample area, comprising a sample stage that can accommodate sample environments of various sizes [Fig. 1, (c)]; and an evacuated detector tank containing six position-

sensitive detector panels mounted on two movable detector carriages [Fig. 1, (d)].

Instrument control for BILBY and sample environments (similar to the majority of instruments operated by ACNS) is provided through the *SINQ Instrument Control System (SICS)* (Könnecke, 1998). *Gumtree* (Lam *et al.*, 2006) provides the user interface for instrument control and workflow for the collection of data.

2.2. Neutron transport and spectrum characteristics

The 20 MW OPAL reactor was designed to deliver an unperturbed thermal neutron flux of $\sim 4 \times 10^{14}$ n cm⁻² s⁻¹ (Robinson & Kennedy, 2002). The cold-neutron source within the OPAL reactor is a 20 l vertical liquid-deuterium thermosiphon with re-entrant cavity in the direction of the cold-neutron guides. The guide (designed in-house and supplied by Swiss Neutronics), designated CG2A (which services BILBY alone), was installed during 2013. It has a cross section of 40 × 100 mm and runs from the primary shutter of the OPAL reactor (with a direct view of the cold source) to the housing of the first neutron chopper. The guide has a radius of curvature of 1500 m (to eliminate γ -radiation and fast neutrons coming from the reactor) up to the secondary shutter, with an additional 4.6 m straight section (called a conditioning guide, to homogenize the neutron distribution across the beam) between the secondary shutter and the housing of the first chopper. The m -coatings of the curved guide section are 3 (top and bottom), and 2 (concave side) and 2.5 (convex side), while

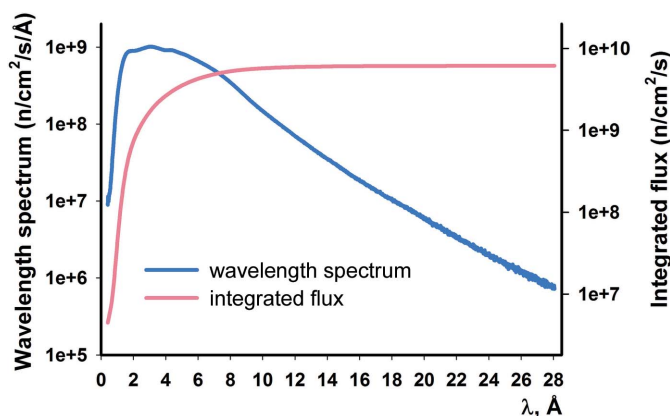


Figure 2 The neutron spectrum (blue curve) and integrated neutron flux (pink curve) measured at the position of the fourth chopper by ToF. The dip in the spectrum around the peak is due to Bragg scattering from the aluminium vacuum windows that terminate each guide section.

the m -coatings of the conditioning guide are 3 on the top and bottom, and 2 on the sides. On the basis of calculations, and to account for the physical constraints applied by the location of the existing neutron guides, the different coatings were chosen to yield a beam divergence that maximizes the number of neutrons accepted by the collimator entrance of the ToF SANS instrument and efficiently transported to the sample. Fig. 2 presents the wavelength spectrum and integrated flux on the CG2A guide measured at the start of the collimator section.

2.3. Choppers

BILBY has four neutron choppers (Airbus SE, formerly EADS Astrium GmbH, Germany) mounted at separations of 4.4 m (distance between choppers 1 and 2), 2.2 m (chopper 2–3 distance) and 1.1 m (chopper 3–4 distance), where each chopper has a radius of ~ 350 mm and an opening window of 120° . The choppers are connected by straight sections of neutron guide (manufactured by S-DH GmbH, Germany), with a cross section of 40×100 mm and an m -coating of 1.2 on all sides. Depending on the wavelength resolution ($\Delta\lambda/\lambda$) required, any pair of choppers can be configured in an optically blind configuration (van Well, 1992) to generate a neutron pulse with $\lambda = 2\text{--}20$ Å. This optically blind configuration is already implemented on D17 (Cubitt & Fragneto, 2002), Figaro (Campbell *et al.*, 2011) and D33 (Dewhurst *et al.*, 2016) (all at ILL), PLATYPUS (James *et al.*, 2006) (ANSTO), and REFSANS (Kampmann *et al.*, 2006) (FRMII, Germany).

As described elsewhere (Dewhurst *et al.*, 2016), an optically blind chopper pair will produce a neutron pulse where $\Delta\lambda/\lambda$ is independent of λ . Briefly, the reason for this is that the relative

uncertainty in the position of the neutrons within each pulse at t_0 (the time at which the first chopper closes and the second chopper opens) is equal to the distance between the chopper pair (ΔD), relative to the total flight distance (D) from the mid-point of the chopper pair to the detector, *i.e.* $\Delta D/D$. For reference, the distance between the midpoint of the chopper pair and the sample position varies between ~ 18.4 and 23.4 m, depending on the chosen chopper pair. For a particular neutron velocity this is equivalent to an uncertainty in time (Δt), relative to the total time of flight (t) to the detector, *i.e.* $\Delta t/t$. Since neutron wavelengths and time of flight are inversely proportional to velocity, it can be shown that $\Delta\lambda/\lambda = \Delta t/t = \Delta D/D$. More simply, $\Delta\lambda/\lambda$ is defined by $\Delta D/D$, which is the reason for the wavelength-resolution flexibility of reactor-based ToF instruments. Fig. 3 illustrates the dependence between the count rate and wavelength resolution for each of the six possible chopper-pair arrangements at two different detector distances. It can be seen that increasing the SDD improves $\Delta\lambda/\lambda$ (*i.e.* at SDD = 6.8 m the accessible values of $\Delta\lambda/\lambda$ range from 4 to 27%, while at SDD = 18 m the accessible values of $\Delta\lambda/\lambda$ range from 3 to 19%).

The transmission of the chopper pair in this configuration is given by $T(\lambda) = \Delta t(\lambda)f$, where $\Delta t(\lambda)$ defines the effective opening time of the double-pair chopper system for each wavelength and f is the chopper frequency (Dewhurst *et al.*, 2016). Thus, as the transmission increases linearly with wavelength, it tends to counteract the low intensity of neutrons at longer wavelengths. The chopper-pair frequency cannot be increased indefinitely to increase transmission, as the effective maximum frequency of the chopper system to avoid frame overlap is limited to f_{\max} (Hz) = $h/Dm_n\lambda_{\max}$ (where h is Planck's constant, D is the distance between the midpoint of the double pair and the detector, m_n is the neutron mass, and λ_{\max} is the maximum wavelength to be transmitted through the system). This frequency ensures that all neutrons with wavelengths up to λ_{\max} arrive at the detector before the next neutron pulse is released. It can also be seen that f_{\max} is limited by the detector distance, and hence a larger SDD results in a lower f_{\max} and a correspondingly lower $T(\lambda)$ (this is the reason for the reduced flux at longer SDD in Fig. 3). The chopper-pair frequency f can, however, be increased by a factor n between 2 and 8, while the remaining choppers rotate at the frequency $f_{\max} = f/n$, permitting the selection of every n th pulse and avoiding frame overlap.

2.4. Wavelength cut-off mirror

The discussion in Section 2.3 assumes that the neutron spectrum entering the chopper system does not contain neutrons with wavelengths greater than λ_{\max} . However, neutrons with longer wavelengths are present at relatively low intensity and are transmitted through the choppers. It is not possible to exclude these longer-wavelength neutrons by changing the frequency of the choppers alone, so they must be removed from the beam. To prevent significant frame overlap of these longer-wavelength neutrons, a cut-off mirror can be inserted into the beam (Copley, 2011; Dewhurst, 2012) to filter

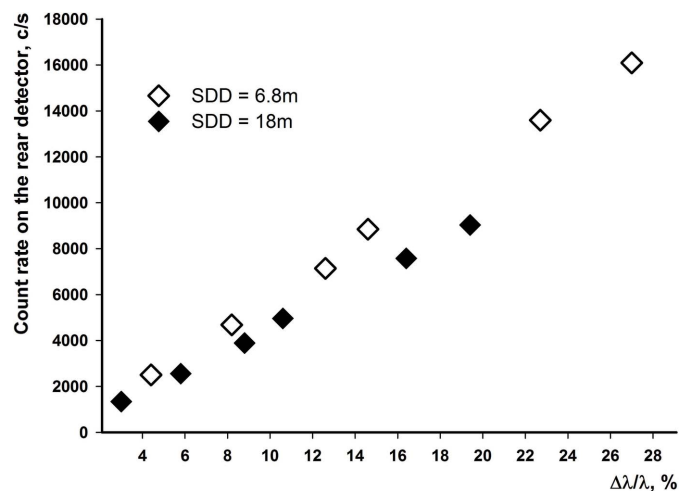


Figure 3

A plot of the count rate of the attenuated direct beam on the rear detector versus $\Delta\lambda/\lambda$, showing a linear relationship for two different sample-to-detector distances (SDD = 6.8 m, shown as hollow diamonds, and SDD = 18.0 m, shown as filled diamonds). It can be seen that there is a decrease in flux of approximately one order of magnitude when moving from a low-resolution ($\Delta\lambda/\lambda \simeq 27\%$, SDD = 6.8 m, chopper pair = 1 and 4 rotating at 6.9 Hz, all pulses reach the sample) to a high-resolution configuration ($\Delta\lambda/\lambda \simeq 3\%$, SDD = 18 m, chopper pair = 3 and 4 rotating at 21.7 Hz, one in four pulses reaches the sample).

them out. The BILBY cut-off mirror (manufactured by S-DH GmbH, Germany), consists of an $m = 3.0$ nickel–vanadium multilayer coating on a 2 mm silicon substrate. The mirror is oriented vertically in a section of the guide between choppers 2 and 3, at an angle of 6° relative to the beam. The left-hand side of the guide section into which the cut-off mirror is inserted (relative to the direction of the beam) has $m = 0.65$ (instead of $m = 1.2$), which eliminates the possibility of double reflection of the long-wavelength neutrons back into the guide. The mirror is designed to attenuate heavily those neutrons with wavelengths greater than 20 \AA (the experimentally determined transmission is $\sim 28\%$ at 20 \AA and $\sim 6\%$ at 23 \AA).

If required, a regular section of guide ($m = 1.2$) can be translated into the beam, in place of the cut-off mirror, depending on the requirements of the experiment.

2.5. Neutron velocity selector

To expand the range of experiments possible on BILBY to include those that require monochromatic neutrons, a neutron velocity selector (NVS) (Airbus SE, Germany) is located between the third and fourth choppers. The NVS or a short section of neutron guide ($m = 1.2$) can be interchangeably translated into the beam. The NVS consists of a turbine constructed from carbon fibre blades, coated with enriched ^{10}B , with a pitch angle of 48.3° and a thickness of 0.4 mm. The rotation speed can be varied between 3150 and 28 600 r min^{-1} in order to select the desired neutron wavelength in the range between 4.5 and 40 \AA , with a wide forbidden interval between 11.5 and 15 \AA (Wagner *et al.*, 1992). The NVS has a nominal $\Delta\lambda/\lambda$ of 10% (FWHM) with a triangular distribution. Fig. 4 shows the neutron brightness as a function of wavelength for

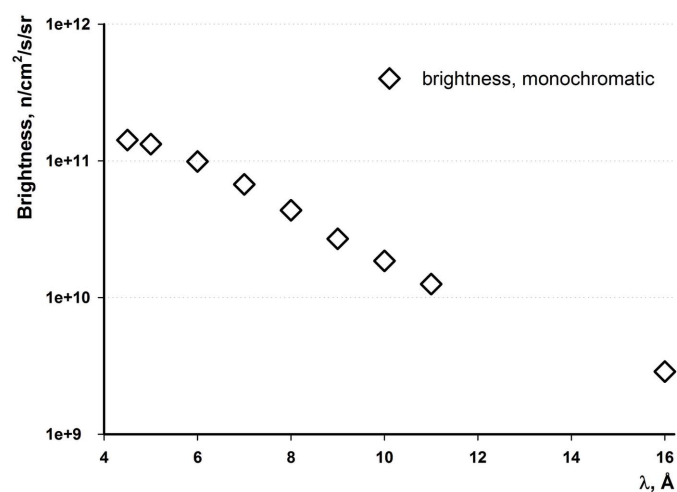


Figure 4
A plot showing the brightness of the neutron beam as a function of wavelength with $\Delta\lambda/\lambda = 10\%$ using the velocity selector (hollow diamonds). For reference, the integrated neutron brightness in ToF mode (set to $\Delta\lambda/\lambda = 10\%$, matching the resolution of the velocity selector) equals $4.7 \times 10^{10} \text{ n cm}^{-2} \text{ s}^{-1} \text{ sr}^{-1}$, which is approximately the same as the neutron brightness of the monochromatic beam at 8.0 \AA . The maximum neutron flux at the sample position using the velocity selector is $2.2 \times 10^7 \text{ n cm}^{-2} \text{ s}^{-1}$ ($\lambda = 4.5 \text{ \AA}$, $\Delta\lambda/\lambda = 10\%$, $L_1 = 2.7 \text{ m}$).

the NVS. Brightness is defined as $[L_1^2 I]/[A_1 A_2]$, where I is the direct beam count rate, L_1 is the source–sample distance, and A_1 and A_2 are the source and sample aperture areas, respectively.

2.6. Attenuators

The attenuators are of a ‘sieve’ type and are located between the last chopper and the start of the collimation system. This type of attenuator was used instead of conventional Plexiglass attenuators owing to the strong wavelength dependence of the transmission of neutrons through Plexiglass. The original attenuator design was composed of two 5 mm borated aluminium plates bolted together. Each plate had thin stripes cut through it, such that when the two plates were bolted together in a perpendicular arrangement a grid of small holes was formed. Testing showed that these plates affected the beam divergence, resulting in the attenuation factor being dependent on the collimation length. The current attenuator design for BILBY is similar to that for D33 (Dewhurst *et al.*, 2016). Each attenuator consists of an array of 0.1–0.4 mm diameter holes in a 0.25 mm thick gadolinium foil forming a 3.5 mm square grid over the entire $40 \times 100 \text{ mm}$ beam cross section. The gadolinium foil is then supported on a 1.5 mm thick sintered B_4C plate with 0.5 mm diameter holes, in the same arrangement as the holes in the gadolinium foil (the B_4C plate faces the beam and thus also serves to reduce the γ -radiation emitted by the gadolinium). These sieves attenuate the neutron beam by a factor between 106 and 1880, which is very close to the theoretical estimates based on the total area for the holes relative to the beam area and appears to be independent of configuration. Specifically, our calibration measurements suggest that the gadolinium foil is thin enough not to affect the beam divergence significantly, making the attenuation factor independent of collimation length, and the density of holes in each attenuator appears to be high enough that the attenuator factor is independent of the collimator aperture size.

2.7. Collimation

The collimation vessel (manufactured by Girod-Sisa, France) contains a variety of elements and is maintained at a pressure of $\sim 10^{-3}$ mbar during operation (1 bar = 100 kPa). The first element upstream inside the collimator is a set of precise B_4C slits (manufactured by ADC, USA) that can be used to shape the beam to any required size. Downstream of the precise slits, the collimation vessel contains eight identical translation tables (Fig. 5).

Mounted onto each table is an aperture wheel carrying a set of five beam-defining apertures followed by an $80 \times 100 \text{ mm}$ aluminium flight tube lined with Mirrobor (80% B_4C in a silicone matrix, manufactured by Mirrotron, Hungary) (Fig. 5, labelled 1), a 2.0 m guide ($m = 1.2$) with $40 \times 40 \text{ mm}$ cross section (Fig. 5, 2) and an empty position to mount future upgrades which will utilize the full cross section of the incoming guide (Fig. 5, 3). The available aperture sizes include $40 \times 100 \text{ mm}$ (rectangular), $40 \times 40 \text{ mm}$ (square), 40 mm

(circular), 20 mm (circular) and 10 mm (circular). Each aperture is made from 3 mm sintered B₄C, with a 7° tapered edge to reduce parasitic scattering. In the original design, the flight tubes were only 42 mm wide, but during commissioning parasitic scattering from the lining of the tube could be seen on the detector. The tubes were thus widened to 80 mm, preventing parasitic scattering from the tube lining passing through the collimation system. The collimator is terminated by a single-crystal sapphire window (125 mm diameter and

4.5 mm thick, with window faces corresponding to the 001 crystal plane; Miracrys LLC, Russia), followed by a removable guard aperture made from borated aluminium, and then by a translation stage with the sample apertures attached.

The combination of aperture and guide elements within the collimator allows the angular divergence of the beam to be varied between ~0.07 and 1.5°, and the brightness of the neutron beam is essentially independent of collimation length at $\sim 1.0 \times 10^{11} \text{ n cm}^{-2} \text{ s}^{-1} \text{ sr}^{-1}$ using the NVS at 6.0 Å with $\Delta\lambda/\lambda = 10\%$ (Fig. 6).

2.8. Sample area

The sample stage is constructed from non-magnetic materials and designed to carry loads up to 600 kg. It can be translated approximately 1.5 m along the beam, ± 0.5 m horizontally across the beam and 0.5 m vertically. Additionally, a rotation stage can be mounted, allowing the sample to be rotated by approximately $\pm 170^\circ$. This large range of motion allows BILBY to accommodate common sample environments (such as linear sample changers) or bulky samples and sample environments (such as large magnets, cryostats, rheometers and furnaces). Samples can be aligned optically using a laser that can be inserted into the guard-aperture mounting.

2.9. Detector vessel and detectors

The detector vessel is 2.5 m in diameter and ~19 m long, manufactured from 8 mm stainless steel, and is maintained between 10^{-4} and 10^{-5} mbar (using a GXS450/4200F dry roughing pump and an STP-XA4503 turbo-molecular pump) during operation. The neutron beam passes through a circular window made from a silicon single crystal with a diameter of 240 mm and thickness of 12 mm (with faces corresponding to the 100 crystal plane; supplied by ISP Optics, USA). The vessel houses two movable detector carriages, with the first carrying a set of ‘curtain’ detectors and the other carrying a single ‘rear’ detector. The whole vessel also sits on a set of rails, allowing it to be translated 1.5 m along the beam. Translation of the vessel varies the size of the sample area to accommodate various pieces of sample environment while minimizing the neutron path through air.

All of BILBY’s detectors are assemblies of 8 mm diameter stainless steel position-sensitive tube detectors (GE Reuter-Stokes, USA) with 0.25 mm walls, filled with ³He (9 atm; 1 atm = 101 325 Pa). The active length of each tube is ~660 mm, where each pixel is 2.81 mm long. The tubes are assembled into ‘8-packs’ with the spacing between tubes being ~0.4 mm, where each 8-pack has its own set of pre-amplifiers. Five 8-packs are mounted on an aluminium frame to form a 320 × 660 mm detector ‘panel’, where each panel contains all the required electronics for independent operation (the electronics are mounted behind each panel shielded by borated aluminium, making each panel ~700 mm deep). The high-voltage (HV) connectors between tubes and preamplifiers are not insulated from the atmosphere; hence a breakdown at an applied detector tube voltage of 1500 V occurs between

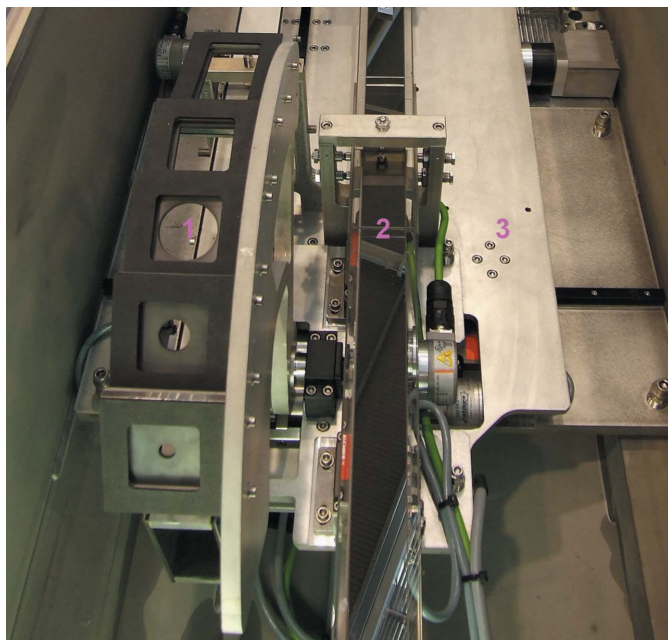


Figure 5
Photograph of the cross section of the integrated collimator section. (1) Apertures plus flight tube. (2) The neutron guide. (3) A spare empty position.

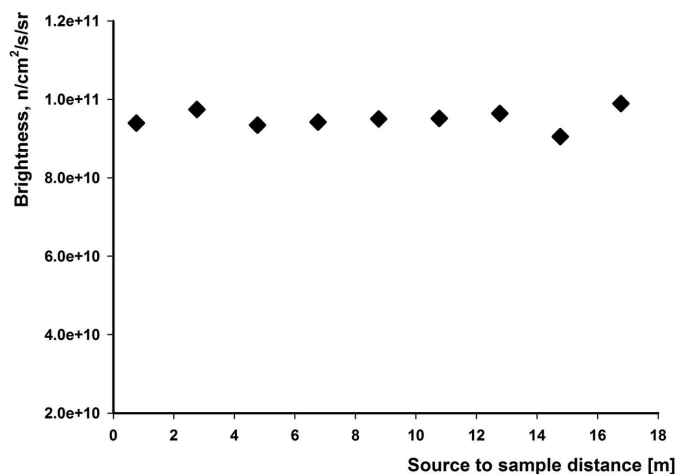


Figure 6
The neutron beam brightness of the neutron velocity selector (6.0 Å, $\Delta\lambda/\lambda = 10\%$) as a function of collimation length. This compares well with the reported brightness of similar instruments: QUOKKA, ANSTO ($\sim 7.7 \times 10^{10} \text{ n cm}^{-2} \text{ s}^{-1} \text{ sr}^{-1}$); NG7, NIST ($\sim 3.1 \times 10^{10} \text{ n cm}^{-2} \text{ s}^{-1} \text{ sr}^{-1}$); D22, ILL ($\sim 3.5 \times 10^{11} \text{ n cm}^{-2} \text{ s}^{-1} \text{ sr}^{-1}$); and D33, ILL ($\sim 4.6 \times 10^{11} \text{ n cm}^{-2} \text{ s}^{-1} \text{ sr}^{-1}$)

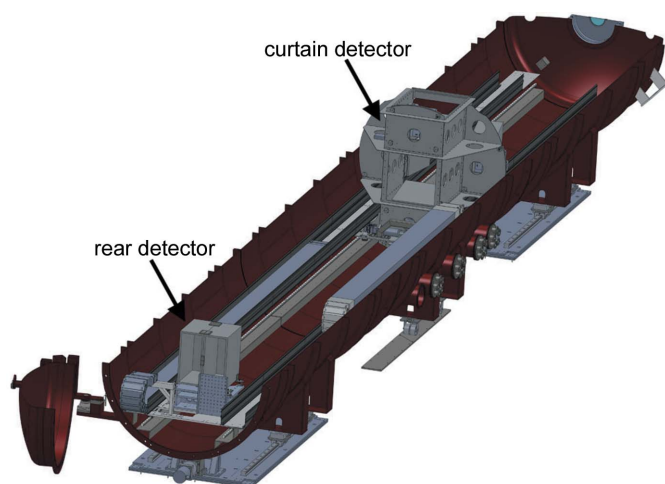


Figure 7

A cut-away image of the BILBY detector vessel, showing the arrangement of the detector carriages. The length of the vessel is 19 m. The beam enters through the silicon window (top right corner), with the curtain detector assembled from four equal panels located closest to this window, and the rear detector, made of two equal panels, positioned furthest from the window.

pressures of 10^{-2} and 600 mbar (Paschen's law). To prevent damage to the electronics due to arcing, the pressure in the tank is maintained below 10^{-4} mbar. As an additional safeguard, ACNS Electrical Engineering and the Detectors and Electronics Group designed and implemented a protection system to lower the detector voltage to a safe level within 10 s if the pressure in the tank moves into the Paschen region. Also, the HV power supplies for the detector electronics shut down automatically if the current jumps by more than 10% above the normal operating value.

The arrangement of the detectors and detector carriage inside the detector vessel is shown in Fig. 7. The rear detector carriage has two detector panels mounted adjacent to each other ($\sim 660 \times 640$ mm). The rear detector carriage can only be translated along the vessel (not across it) and can be positioned anywhere between 4.0 and 18.4 m from the silicon entrance window. The curtain detector carriage has two detector panels mounted vertically (the left and right curtain detectors) and two detector panels mounted horizontally (the upper and lower curtain detectors). Each panel is tilted by 10° from perpendicular to the beam to prevent shadowing of adjacent tubes, and can be translated by up to 380 mm from the beam centre line. The curtain detector carriage can be translated such that the left and right curtain detectors are within 100 mm of the silicon entrance window (the upper and lower curtains are mounted 1000 mm behind the left and right curtains).

3. Instrument calibration

3.1. Detector dead time

The GE Reuter–Stokes detectors have a specified dead time of 10% at a count rate of 50 kHz per tube. While the time-averaged count rate for a pulsed beam may not approach this

value, the instantaneous count rate (at the peak wavelength) may well exceed it. As no dead-time correction is currently applied to the data, it is important not to enter a regime where the dead time is significant. To keep the detector dead time below the chosen threshold of 1%, the maximum instantaneous count rate on any given tube is kept below ~ 5 kHz, and this is monitored using the acquisition software. In our experience, instantaneous count rates per tube in excess of ~ 5 kHz are only observed for direct-beam measurements, and the count rate is reduced during configuration through selection of an appropriate attenuator. Where instantaneous count rates exceed ~ 5 kHz per tube for sample scattering, we would first consider reducing the sample thickness, and if this is not practical we would modify the collimation configuration.

3.2. Detector spatial corrections

The mounting of the 8-packs to the preamplifiers results in small deviations in the alignment of the tubes. Additionally, the active area and response of each tube may differ slightly. To correct for spatial inhomogeneity on each detector panel, absorbing masks were placed over the detectors and the strong incoherent signal from water was collected. These patterns were analysed to determine the relative position of each tube, and these relative shifts are recorded in a separate file and applied during data reduction.

3.3. Detector panel positions

The absolute positions of the detectors were initially defined using a laser tracker (FARO, USA) to an estimated accuracy of ~ 2 mm (the primary cause of the limited accuracy is due to the placement of the target nests). This is well above the accuracy of the absolute encoders used on the instrument axes, which is below 0.02 mm. To define the positions of the detectors more accurately, they have been calibrated against a silver behenate standard. This material has a well defined crystalline structure with a large unit-cell axis, making it appropriate for the calibration of small-angle X-ray and neutron scattering instruments (Gilles *et al.*, 1998; Huang *et al.*, 1993). A comprehensive set of data was collected in ToF mode at several sample-to-detector distances and curtain positions. The corrections to the detector position based on the silver behenate peaks are recorded in the instrument definition file.

3.4. Choppers and NVS

While the design parameters of the NVS are well defined, the way in which it is mounted in the beam may affect the apparent pitch angle and wavelength resolution. With respect to the neutron choppers, there may be some uncertainty in the angle of the chopper when the framing signal is sent. The method used on BILBY to calibrate the apparent pitch angle and wavelength resolution of the NVS and the offset angle of each chopper is similar to that outlined elsewhere (Dewhurst *et al.*, 2016), except that instead of a step-by-step process, all parameters are refined simultaneously. Attenuated direct-beam measurements are made using the NVS and one chopper at a time, varying the NVS speed, the rotating

chopper, the chopper frequency and the detector distance. These data are fed into a custom-written least-squares optimization program that refines the chopper and NVS parameters by minimizing the difference between the experimental and calculated spectrum shapes. In all cases, the difference between the expected and optimized parameters is currently negligible and no correction is applied.

4. Data format, reduction, resolution and corrections

4.1. Data format

The BILBY data-acquisition server records data in what is referred to as list or event mode for both ToF and monochromatic configurations. In event mode, the coordinates and arrival time (with a resolution of 100 ns) of each neutron detection event are recorded, instead of histogramming each detection event into a given pixel and time bin. The frame trigger, which defines the time of origin for each pulse, is also written to this file. The frame-trigger signal is generated by a sensor inside the drive unit as the centre of each chopper window passes through the beam centre. This signal can be taken from any one of the four neutron choppers.

Collection of data in event mode provides significant flexibility during processing, allowing the user to process time subsets. Successful reduction of data also requires knowledge of the instrument configuration. To ensure that both the neutron data and configuration are correctly associated, BILBY data files are a tar archive composed of two binary files. The first is the event-mode data and the second a NeXus HDF file (Könnecke *et al.*, 2015), where the latter contains a comprehensive description of the instrument setup, sample details, sample-environment parameters, and reactor and cold-source details.

4.2. Data reduction

The *Mantid* software suite (Arnold *et al.*, 2014) is used to reduce BILBY ToF data (one- or two-dimensional) on an absolute scale against the direct beam intensity, correcting for sample thickness, background scattering, transmission, gravity and solid angle (Seeger & Hjelm, 1991; Sokolova *et al.*, 2016; Heenan *et al.*, 1997). Equally, the reduction software can be used to reduce monochromatic data collected from BILBY. Transmission measurements are made on BILBY by measuring the attenuated beam spectrum on the rear detector. The transmission spectrum of a sample is divided by that of the empty beam and a function is fitted to the result (typically a third-order polynomial is used, but other functions are also available). The neutron trajectories for all wavelengths are corrected relative to the optical beam centre of the instrument, but appropriate masking is required to ensure that transmitted neutrons of longer wavelengths, which have fallen significantly under gravity and are not absorbed by the beamstop, do not cause artefacts in the reduced data. The resolution function for each q value is also estimated by *Mantid* (fourth column of the one-dimensional data file)

(Mildner & Carpenter, 1984), assuming a constant $\Delta\lambda/\lambda$, which is discussed further in Section 4.4.

It is envisaged that a number of features will be added to the BILBY data-reduction procedure in the future. According to a number of test measurements, the response of all detector pixels is very uniform. Therefore, no correction is currently applied for either pixel efficiency or parallax, and instead shadowed pixels and pixels that show an abnormal response can be masked during the data-reduction procedure. Another feature that we hope to add in the near future is the ability to refine the position of the beam centre (currently a single beam centre is defined in the instrument configuration file for all instrument setups). While this may appear to be a serious limitation, at present the fixed beam position appears to perform adequately. Deviation of the beam centre is regularly monitored by reduction of scattering data on the rear detector in four separate quadrants and each curtain separately, assessing the similarity between the curves.

The final item is normalizing the data to the source intensity and, while not difficult to implement, this requires a proportional beam monitor. The original beam monitor (low-efficiency dual-anode gas proportional counter manufactured by Ordela, USA) installed on BILBY appears to be sensitive to γ -radiation and did not produce a signal proportional to the beam intensity, so we currently normalize to time, which means that our absolute scaling and transmissions are sensitive to changes in flux (caused for example by fluctuations in reactor power). From our experience, the OPAL reactor is very stable and the flux fluctuations are usually less than 2% over the course of an experiment (which typically spans 3–4 days), and this is currently monitored by making a number of measurements of the direct-beam transmission over the course of an experiment.

On a practical note, we encourage users to reduce their data over small wavelength ranges and overlay them for at least one representative sample. This procedure allows users to identify issues quickly (caused by, for example, inelastic scattering, multiple scattering and Bragg-edge effects in the transmission) and, if required, truncate the wavelength range used in the reduction of their data. Such issues are not necessarily immediately obvious and often remain undetected in monochromatic mode, so careful analysis of ToF data provides a means of quickly diagnosing and identifying these effects.

4.3. Multiple scattering

Strong scatterers are prone to coherent ‘multiple scattering’, whereby an elastically scattered neutron is re-scattered elastically as it passes through a sample. The probability of a neutron being multiply scattered is wavelength dependent, proportional to λ^2 (Sabine & Bertram, 1999). Methods have been proposed to correct the distortion of the scattering data caused by multiple scattering (Schelten & Schmatz, 1980), but where possible it is best to avoid the effect altogether. Typically, as a guide to determining whether a sample will display the effects of multiple scattering, in

transmission geometry the number of counts from scattered neutrons can be compared with the total number of counts on the detector. If the percentage of scattered neutrons is greater than ~10% of the total counts, then it is likely the sample will see the effects of multiple scattering. Because BILBY uses a range of neutron wavelengths, if multiple scattering is significant then the extent of the effect will increase at longer wavelengths and will manifest itself in the low- q portion of the curve. By reducing and overlaying scattering using different wavelength ranges, it is possible to identify the affected wavelengths and exclude them from the reduction procedure. In cases where the effects of multiple scattering are present, longer wavelengths will be excluded from the data reduction, so care should be taken to ensure that the required q range is still accessible using a truncated wavelength range. Where multiple scattering affects the shorter wavelengths, alternative strategies such as sample dilution or reducing the sample thickness need to be investigated.

4.4. Instrument resolution

In general, the instrumental resolution has contributions from both the geometry and the wavelength distribution. The geometric component is dictated by the collimation length, the sample and source apertures, and the position of the detectors. The wavelength distribution is dictated by the method used to select the neutrons – for BILBY this is either using the NVS or using the choppers. For the NVS, $\Delta\lambda/\lambda \simeq 10\%$, and for the choppers set in an optically blind configuration, the wavelength resolution is given by $\Delta\lambda/\lambda = \Delta D/D$ (Section 2.3) (van Well & Fredrikze, 2005).

The q resolution at each q value is currently calculated in *Mantid* using the routine *TOFSANSResolutionByPixel* Version 1 (for the current version, see the Algorithm Descriptions page on the *Mantid* web site at <http://www.mantidproject.org/Documentation>), which takes the

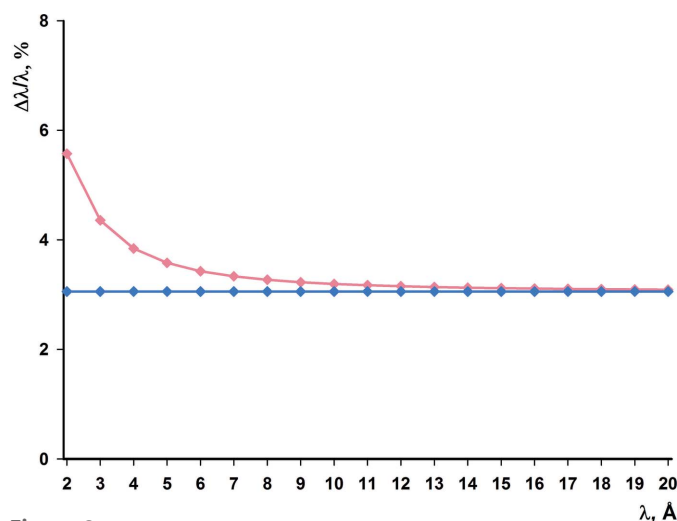


Figure 8 Resolution estimated as $\Delta\lambda/\lambda = \Delta D/D$ (blue) and as described by van Well & Fredrikze (2005) (pink) for SDD = 18 m and a blind-pair chopper frequency of 21 Hz.

instrument geometry and a constant wavelength distribution to estimate the q resolution. For spallation sources, the moderator time spread is also a parameter in this routine, but this is not relevant for reactor sources and as such is set to zero for the reduction of BILBY data.

While the geometric/angular component is correctly estimated, the wavelength resolution is currently a single input parameter in the data-reduction script, and thus, while accurate for the NVS mode (note $\Delta\lambda/\lambda$ here is quoted as the FWHM of a triangular function), it is only an estimate for the ToF mode. For the ToF mode, the wavelength resolution (note $\Delta\lambda/\lambda$ here is quoted as the full width of an approximately rectangular function) is dependent on the length of the neutron flight path, and neutrons detected at the curtain detectors (close to the sample) will have a coarser wavelength resolution. Furthermore, low chopper frequencies cause broadening of the pulse because of the finite time it takes the leading and trailing edges of the chopper window to cross the beam (Δt_g), leading to a degradation of the wavelength resolution, particularly at short wavelengths (Fig. 8).

This effect should be considered when calculating the resolution function. In time, the plan is to implement more accurate estimates of the resolution function that account for these effects (Nelson, 2013).

4.5. Incoherent elastic and inelastic scattering

Incoherent scattering increases the background intensity in a SANS experiment, and the most common source is from hydrogen (^1H). Because the effect can be large compared with the coherent small-angle scattering signal, it reduces the signal-to-noise ratio in the data. The contribution from

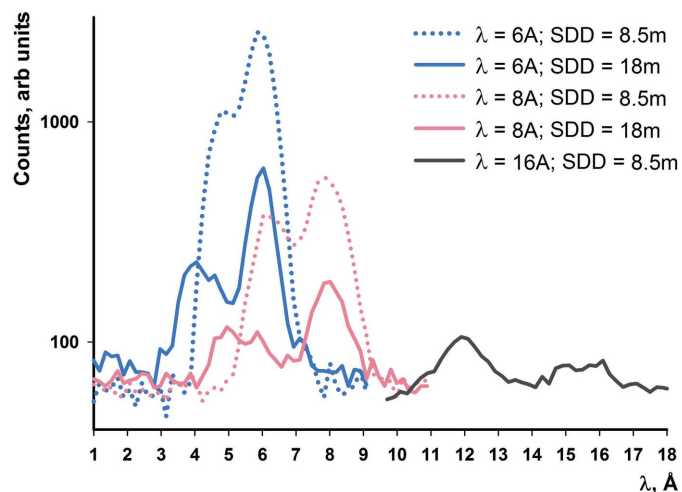


Figure 9 The wavelength spectrum measured in scattering geometry with the simultaneous use of the NVS and choppers. The neutron beam has passed through a 1.0 mm sample of H_2O at 293 K. A significant portion of the incoherently scattered neutrons have been thermalized (increased in velocity), and the proportion is dependent on the incident neutron wavelength. The position of the elastic peak does not change with SDD but that of the thermalized peak does, because the average velocity of thermalized neutrons is dependent on the SDD. The data have not been corrected for the detector efficiency.

incoherent elastic scattering is uniform for a given wavelength (Shibayama *et al.*, 2009), so its contribution can be removed by the subtraction of an appropriate and carefully measured background. However, a significant number of neutrons scattering incoherently from hydrogenous samples are also thermalized.

Fig. 9 clearly demonstrates this very effect: an incoming monochromatic neutron beam, scattered by a 1 mm H₂O sample at 293 K, comprises not only neutrons of the incident wavelength, but also thermalized neutrons of shorter wavelength. Note that the wavelength calculated by ToF for the thermalized neutrons is based on the average neutron velocity: neutrons travel at a given velocity between the choppers and the sample, but are thermalized at the sample position and travel at a higher velocity between the sample and the detector. Thus, the ‘apparent’ wavelength (calculated from the average velocity) will lie between the incident and final wavelengths. Furthermore, the apparent wavelength depends on the SDD and hence the proportion of the neutron flight path before and after the sample. Calculations (not shown here) indicate that the wavelength of the thermalized neutrons is ~ 2 Å in all cases, consistent with results from other facilities (Hjelm, 1988; Rennie & Heenan, 1992; Barker & Mildner, 2015; Ghosh & Rennie, 1990, 1999; Lindner, 2000; Do *et al.*, 2014).

Additionally, as the detectors are positioned at different distances from the sample, thermalized neutrons will be registered in different wavelength or velocity bins, thus becoming q dependent. In our experience with dilute samples such as glucose isomerase (Fig. 11), these effects appear to subtract out if an appropriate background measurement is taken. More problematic samples are likely to be concentrated or condensed samples, where the substance of interest causes

significant inelastic and incoherent scattering and there is no suitable background measurement to subtract. There are plans to investigate this effect in greater depth, to come up with a method for identifying and removing this effect from ToF scattering data.

5. Instrument performance

The two banks of multi-tube detectors extend the dynamic q range on BILBY to $q_{\max}/q_{\min} \simeq 100$ in a monochromatic configuration and to as much as $q_{\max}/q_{\min} \simeq 1500$ in a ToF configuration. The enhanced dynamic q range compensates somewhat for the fact that the brightness for a ToF configuration is approximately half that obtained in a monochromatic configuration at 6 Å for a comparable resolution setting (see Fig. 4). To date, $\sim 95\%$ of the user experiments have been conducted in ToF mode, with $\sim 25\%$ of these requiring high-resolution ToF settings. The velocity selector is used primarily for instrument calibration and for difficult specialist experiments that do not require an extended q range, but it is also available in case of technical problems with the chopper system.

5.1. Standard latex spheres

Fig. 10(a) shows scattering data measured in both TOF and monochromatic modes from a sample of spherical polystyrene latex particles with a diameter of 700 Å dispersed in 100% D₂O, where data from all detector panels have been merged to yield the $I(q)$ data. This material has previously been used for round-robin experiments to compare the performance of several instruments worldwide (Rennie *et al.*, 2013), although the data presented here show evidence of some aggregation of

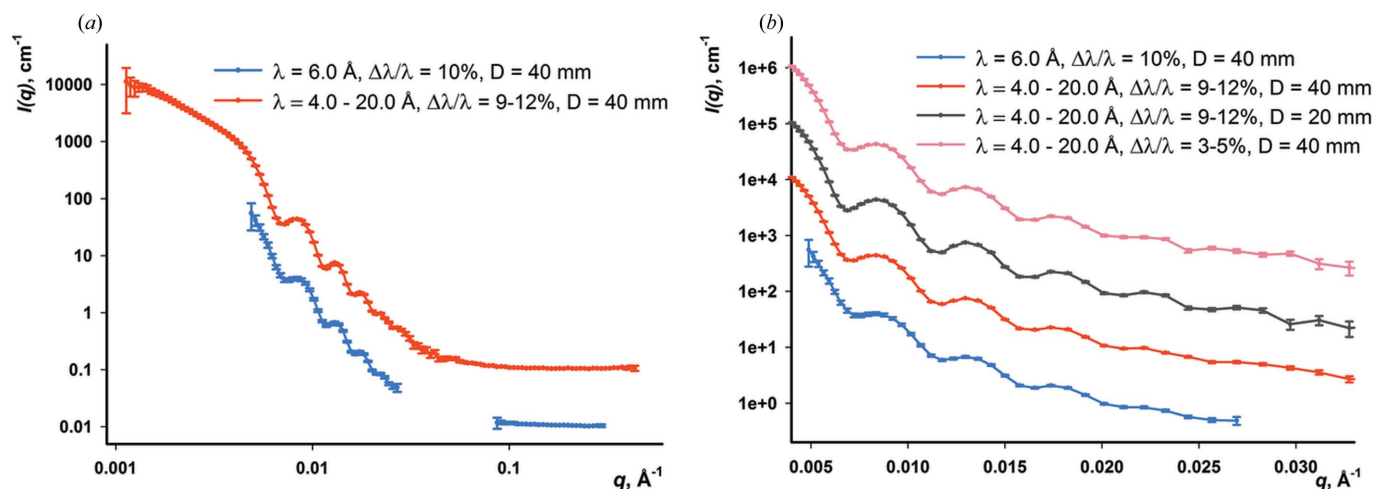


Figure 10

Scattering data collected from polystyrene latex spheres ($\sim 0.5\%$ w/v) in D₂O with a 1 mm path length and collected for 1 h. (a) A comparison showing the large q range of the ToF measurement (red curve) relative to the monochromatic measurements (blue curve), conducted at identical detector settings (the red curve has been offset vertically for clarity by a factor of 10). (b) The effect of changing the resolution setting of the instrument. The red curve was measured in ToF mode with a wavelength resolution of $\Delta\lambda/\lambda \simeq 9\%$ on the rear detector and $\Delta\lambda/\lambda \simeq 12\%$ on the curtain detector. The dark-grey curve shows data collected using the same chopper settings but with the collimation aperture diameter D reduced from 40 to 20 mm. The pink curve shows data measured using 40 mm collimation apertures, but with an improved wavelength resolution of $\Delta\lambda/\lambda \simeq 3.5\%$ on the rear detector and $\Delta\lambda/\lambda \simeq 5.5\%$ on the curtain detector. The blue curve shows data measured in monochromatic mode at 6.0 Å with $\Delta\lambda/\lambda \simeq 10\%$ (curves have been offset vertically for clarity by a factor of 10 for the red curve, 10² for the dark-grey curve and 10³ for the pink curve).

the latex particles. It is immediately obvious [see Fig. 10(a)] that the accessible q range in monochromatic mode is smaller than that in ToF mode. With the collimation length and detector distance fixed, the pink, dark-grey and red scattering curves shown in Fig. 10(b) are collected at different ToF settings (varying the collimation aperture size and wavelength resolution), and the blue curve in the same panel shows the data collected in a monochromatic setting at 6.0 Å. While the ToF data span the entire q range, it can be seen that the monochromatic setup leaves a gap in the $I(q)$ data for this detector setup. Comparing the ToF data [Fig. 10(b)], it can be seen that reducing the source aperture improves the angular resolution, and this difference is seen in the low- q regions of the dark-grey and red curves. In turn, improving the wavelength resolution increases the number of form-factor oscillations in the high- q region, seen in the pink pattern relative to the red pattern.

5.2. Glucose isomerase

Among structural biologists, there is a preference for conducting SANS experiments on biological macromolecules with monochromatic instruments at reactor sources. There are a variety of reasons for this but, in part, it is because solutions of biological samples are inherently hydrogen rich and, as discussed in Section 4.5, incoherent/inelastic scattering from hydrogen-rich samples can cause problems for ToF data reduction. To investigate whether the effects from incoherent/inelastic scattering could be successfully subtracted for dilute but hydrogen-rich samples, measurements were made on glucose isomerase (Kozak, 2005). Data were collected on QUOKKA ($\lambda = 5.0$ Å, $\Delta\lambda/\lambda \simeq 10\%$) and BILBY ($\lambda = 2.0$ – 20.0 Å, $\Delta\lambda/\lambda \simeq 10\%$), and the BILBY ToF data show an excellent correspondence to the monochromatic data

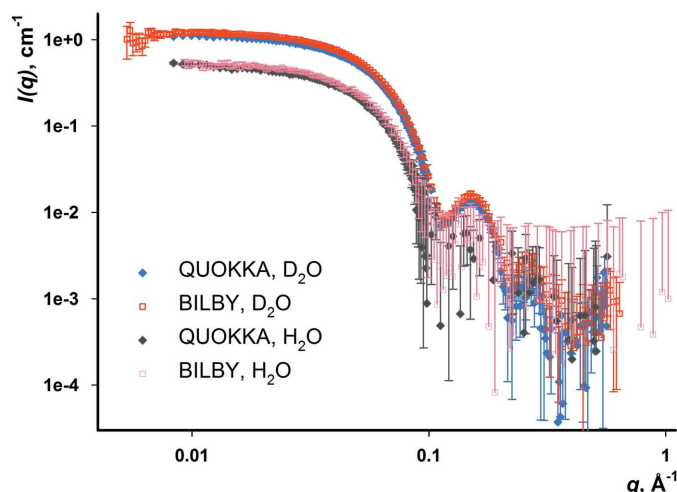


Figure 11 Data collected from monodisperse solutions of glucose isomerase (6.6 mg ml⁻¹, 173 kDa) with $\Delta\lambda/\lambda \simeq 10\%$ on QUOKKA (in H₂O for 2 h: dark-grey curve; in D₂O for 50 min: blue curve) and on BILBY in ToF mode (in H₂O for 2 h: pink curve; in D₂O for 1 h: red curve). The displayed q range for the samples in H₂O has been truncated because of high noise levels. The path length for all samples was 1 mm.

collected on QUOKKA (Fig. 11). These encouraging results show that ToF measurements from biological samples can yield high-quality data that are comparable to those collected on monochromatic instruments.

5.3. Liquid crystals

Resolving peaks in the small-angle regime can be a difficult task on SANS instruments, as they are generally broadened because of instrument smearing. Fig. 12 shows the scattering pattern of monoolein in excess D₂O, which forms a diamond-type bicontinuous cubic phase at room temperature. The data were measured for 10 min in velocity-selector mode with a wavelength resolution of $\Delta\lambda/\lambda \simeq 10\%$ (Fig. 12, blue curve) and in high-resolution ToF mode with $\Delta\lambda/\lambda \simeq 5\%$ (Fig. 12, red curve for data between 3–18 Å) in an otherwise identical setup. The collimation length was 6.8 m, the sample-to-rear-detector distance was 6 m, and the distances from the sample to the two sets of detector curtains were 1.8 and 2.8 m, respectively. While the flux in the high-resolution ToF mode is approximately five times lower than that in the velocity-selector mode, it is clear that the superior $\Delta\lambda/\lambda$ resolution significantly sharpens the peaks, and four (or with better statistics, five) clear peaks can be resolved.

6. Conclusions

The past eight years have seen the development of the BILBY instrument from an idea to a productive neutron scattering instrument. The requirement for BILBY to have flexibility with regard to wavelength resolution and a large dynamic q range has been met by the ToF design, in which the wavelength resolution can be varied between 3 and 30% and the dynamic q range is as high as $q_{\max}/q_{\min} \simeq 1500$. Since its

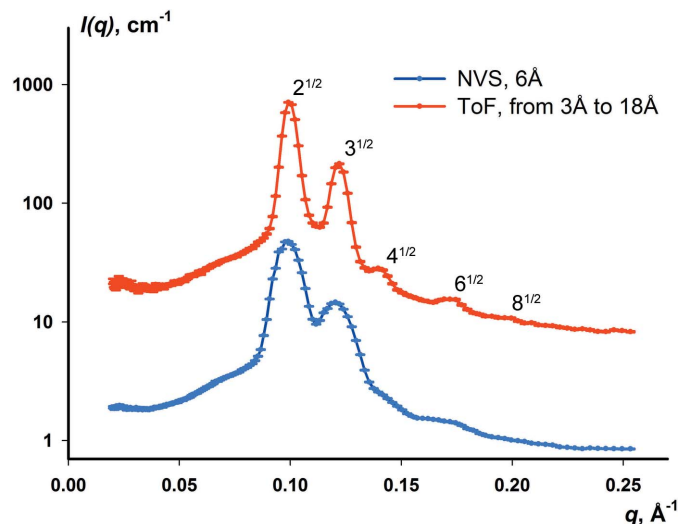


Figure 12 Small-angle diffraction data from monoolein in excess D₂O, forming a diamond-type bicontinuous cubic phase, collected for 10 min in velocity-selector mode ($\lambda = 6.0$ Å, $\Delta\lambda/\lambda \simeq 10\%$, blue curve) and in high-resolution ToF mode ($\lambda = 3.0$ – 18.0 Å, $\Delta\lambda/\lambda \simeq 5\%$, red curve, offset vertically for clarity by a factor of 10).

inclusion in the Australian Centre for Neutron Scattering user programme in 2016, BILBY has contributed to a wide variety of scientific projects in fields such as chemistry, biology and physics, with diverse samples including metals, cokes (Sakurovs *et al.*, 2018), cements (Loy *et al.*, 2017, 2018), polymers (Baek *et al.*, 2017; Dae Jang *et al.*, 2018), peptides, mesoporous materials (Jiang *et al.*, 2018) and lipids/surfactants (Iqbal *et al.*, 2017; Kelleppan *et al.*, 2018; Lin *et al.*, 2016; Marlow *et al.*, 2018; McCoy *et al.*, 2018; Moore *et al.*, 2018). BILBY's complementarity to the other SANS instruments at ANSTO has been demonstrated. Its particular strength lies in the collection of kinetic data on samples and its high wavelength resolution, and it is even being used to carry out Bragg-edge neutron imaging experiments (Salvemini *et al.*, 2017; Sokolova *et al.*, 2016). In the near future we will implement a number of upgrades to the instrument and data-reduction software that will improve the reliability of the instrument, while also improving the usability of the data-reduction workflow.

Acknowledgements

We thank Rob Robinson and Frank Klose for securing funding for, and overseeing, the BILBY project, and the Instrument Advisory Team for their input and guidance in the early stages of the project. We also thank Shane Kennedy for his constant support, help with recording the wavelength spectrum presented in Fig. 2, and constant interest in the BILBY project. We would like to acknowledge Charles Dewhurst, John Barker, Charles Glinka, John Copley, Richard Heenan, Robert Knott and William Hamilton for their advice, instruction and fruitful discussions during the BILBY construction and commissioning project. We are grateful for the support of the Electronics and Computing Group (especially Mark Lesha, Ferdi Franceschini, Norman Xiong, Nick Hauser and David Mannicke), the Mechanical Group (especially Scott Olsen, Merv Perry, Martin Jones and David Roach) and the Electrical Engineering Team (especially Paul Barron, David Federici, Dan Bartlett and Laurence Heffernan).

References

- Arnold, O., Bilheux, J. C., Borreguero, J. M., Buts, A., Campbell, S. I., Chapon, L., Doucet, M., Draper, N., Ferraz Leal, R., Gigg, M. A., Lynch, V. E., Markvardsen, A., Mikkelsen, D. J., Mikkelsen, R. L., Miller, R., Palmen, K., Parker, P., Passos, G., Perring, T. G., Peterson, P. F., Ren, S., Reuter, M. A., Savici, A. T., Taylor, J. W., Taylor, R. J., Tolchenov, R., Zhou, W. & Zikovsky, J. (2014). *Nucl. Instrum. Methods Phys. Res. A*, **764**, 156–166.
- Baek, P., Aydemir, N., An, Y., Chan, E., Sokolova, A., Nelson, A., Mata, J., McGillivray, D., Barker, D. & Trivas-Sejdic, J. (2017). *Chem. Mater.* **29**, 8850–8858.
- Barker, J. G. & Mildner, D. F. R. (2015). *J. Appl. Cryst.* **48**, 1055–1071.
- Campbell, R. A., Wacklin, H. P., Sutton, I., Cubitt, R. & Fragneto, G. (2011). *Eur. Phys. J. Plus*, **126**, 1–22.
- Carpenter, M. & Faber, J. (1978). *J. Appl. Cryst.* **11**, 464–465.
- Copley, J. R. D. (2011). *Nucl. Instrum. Methods Phys. Res. A*, **659**, 403–410.
- Cubitt, R. & Fragneto, G. (2002). *Appl. Phys. A*, **74**, s329–s331.
- Dae Jang, J., Bang, J., Soo Han, Y., Sokolova, A. & Kim, T.-H. (2018). *Physica B*, **551**, 184–190.
- Dewhurst, C. D. (2012). *Nucl. Instrum. Methods Phys. Res. A*, **683**, 16–23.
- Dewhurst, C. D., Grillo, I., Honecker, D., Bonnaud, M., Jacques, M., Amrouni, C., Perillo-Marcone, A., Manzin, G. & Cubitt, R. (2016). *J. Appl. Cryst.* **49**, 1–14.
- Do, C., Heller, W. T., Stanley, C., Gallmeier, F. X., Doucet, M. & Smith, G. S. (2014). *Nucl. Instrum. Methods Phys. Res. A*, **737**, 42–46.
- Ghosh, R. E. & Rennie, A. R. (1990). *Inst. Phys. Conf. Ser.* **107**, 233–244.
- Ghosh, R. E. & Rennie, A. R. (1999). *J. Appl. Cryst.* **32**, 1157–1163.
- Gilbert, E. P., Schulz, J. C. & Noakes, T. J. (2006). *Physica B*, **385–386**, 1180–1182.
- Gilles, R., Keiderling, U. & Wiedenmann, A. (1998). *J. Appl. Cryst.* **31**, 957–959.
- Heenan, R. K., Penfold, J. & King, S. M. (1997). *J. Appl. Cryst.* **30**, 1140–1147.
- Heenan, R. K., Rogers, S. E., Turner, D., Terry, A. E., Treadgold, J. & King, S. M. (2011). *Neutron News*, **22**(2), 19–21.
- Hjelm, R. P. (1988). *J. Appl. Cryst.* **21**, 618–628.
- Huang, T. C., Toraya, H., Blanton, T. N. & Wu, Y. (1993). *J. Appl. Cryst.* **26**, 180–184.
- Iqbal, M., Li, C., Wood, K., Jiang, B., Takei, T., Dag, Ö., Baba, D., Nugraha, A. S., Asahi, T., Whitten, A. E., Hossain, M. S. A., Malgras, V. & Yamauchi, Y. (2017). *Chem. Mater.* **29**, 6405–6413.
- Ishikawa, Y., Furusaka, M., Niimura, N., Arai, M. & Hasegawa, K. (1986). *J. Appl. Cryst.* **19**, 229–242.
- James, M., Nelson, A., Brule, A. & Schulz, J. C. (2006). *J. Neutron Res.* **14**, 91–108.
- Jiang, B., Guo, Y., Kim, J., Whitten, A. E., Wood, K., Kani, K., Rowan, A. E., Henzie, J. & Yamauchi, Y. (2018). *J. Am. Chem. Soc.* **140**, 12434–12441.
- Kampmann, R., Haese-Seiller, M., Kudryashov, V., Nickel, B., Daniel, C., Fenzl, W., Schreyer, A., Sackmann, E. & Rädler, J. (2006). *Physica B*, **385–386**, 1161–1163.
- Kelleppan, V. T., Moore, J. E., McCoy, T. M., Sokolova, A. V., de Campo, L., Wilkinson, B. L. & Tabor, R. F. (2018). *Langmuir*, **34**, 970–977.
- Könnecke, M. (1998). *Physica B*, **241–243**, 124–126.
- Könnecke, M., Akeroyd, F. A., Bernstein, H. J., Brewster, A. S., Campbell, S. I., Clausen, B., Cottrell, S., Hoffmann, J. U., Jemian, P. R., Männicke, D., Osborn, R., Peterson, P. F., Richter, T., Suzuki, J., Watts, B., Wintersberger, E. & Wuttke, J. (2015). *J. Appl. Cryst.* **48**, 301–305.
- Kozak, M. (2005). *J. Appl. Cryst.* **38**, 555–558.
- Kuklin, A., Islamov, A., Balasoiu, M., Murugova, T. & Gordeliy, V. (2012). *J. Phys. Conf. Ser.* **351**, 012001.
- Lam, T., Götz, A., Franceschini, F. & Hauser, N. (2006). *J. Neutron Res.* **14**, 167–175.
- Lin, S. T., Lin, C. S., Chang, Y. Y., Whitten, A. E., Sokolova, A., Wu, C. M., Ivanov, V. A., Khokhlov, A. R. & Tung, S. H. (2016). *Langmuir*, **32**, 12166–12174.
- Lindner, P. (2000). *J. Appl. Cryst.* **33**, 807–811.
- Loy, C. W., Matorie, K. A., Zainuddin, N., Whitten, A. E., Rehm, C., de Campo, L., Sokolova, A. & Schmid, S. (2017). *Powder Diffraction*, **32**(Suppl. S2), S61–S65.
- Loy, C. W., Whitten, A. E., de Campo, L., Appadoo, D., Zainuddin, N., Matorie, K. A., Rehm, C., Sokolova, A., Wang, C., Xia, Q., Whittle, T. A. & Schmid, S. (2018). *Physica B*, **551**, 287–290.
- Marlow, J. B., Pottage, M. J., McCoy, T. M., De Campo, L., Sokolova, A., Bell, T. D. M. & Tabor, R. F. (2018). *Phys. Chem. Chem. Phys.* **20**, 16592–16603.
- McCoy, T. M., de Campo, L., Sokolova, A. V., Grillo, I., Izgorodina, E. I. & Tabor, R. F. (2018). *Phys. Chem. Chem. Phys.* **20**, 16801–16816.
- Mildner, D. F. R. (1978). *Nucl. Instrum. Methods*, **151**, 29–39.

- Mildner, D. F. R. & Carpenter, J. M. (1984). *J. Appl. Cryst.* **17**, 249–256.
- Moore, J. E., McCoy, T. M., de Campo, L., Sokolova, A. V., Garvey, C. J., Pearson, G., Wilkinson, B. L. & Tabor, R. F. (2018). *J. Colloid Interface Sci.* **529**, 464–475.
- Nelson, A. R. J. (2013). *J. Appl. Cryst.* **46**, 1338–1346.
- Rehm, C., Brûlé, A., Freund, A. K. & Kennedy, S. J. (2013). *J. Appl. Cryst.* **46**, 1699–1704.
- Rehm, C., de Campo, L., Brûlé, A., Darmann, F., Bartsch, F. & Berry, A. (2018). *J. Appl. Cryst.* **51**, 1–8.
- Rennie, A. R. & Heenan, R. K. (1992). *International Seminar on Structural Investigations at Pulsed Neutron Sources*, 1–4 September 1992, Dubna, Russia, pp. 254–260. Dubna, Moscow: Publishing Department of the Joint Institute for Nuclear Research.
- Rennie, A. R., Hellsing, M. S., Wood, K., Gilbert, E. P., Porcar, L., Schweins, R., Dewhurst, C. D., Lindner, P., Heenan, R. K., Rogers, S. E., Butler, P. D., Krzywon, J. R., Ghosh, R. E., Jackson, A. J. & Malfois, M. (2013). *J. Appl. Cryst.* **46**, 1289–1297.
- Robinson, R. A. & Kennedy, S. J. (2002). *Physica B*, **311**, 44–49.
- Sabine, T. M. & Bertram, W. K. (1999). *Acta Cryst.* **A55**, 500–507.
- Sakurovs, R., Koval, L., Grigore, M., Sokolova, A., Ruppert, L. F. & Melnichenko, Y. B. (2018). *Int. J. Coal Geol.* **186**, 126–134.
- Salvemini, F. F., Luzin, V., Grazi, F., Avdeev, M., Gatenby, S. & Kim, M.-J. (2017). The Ninth International Conference on the Beginnings of the Use of Metal and Alloys (BUMA9), 16–19 October 2017, Busan, Republic of Korea, Abstract P00035. http://buma9.org/wp-content/uploads/2017/10/BUMA9_AbstractBook.docx%EC%B5%9C%EC%A2%85.pdf.
- Schelten, J. & Schmatz, W. (1980). *J. Appl. Cryst.* **13**, 385–390.
- Seeger, P. A. & Hjelm, R. P. (1991). *J. Appl. Cryst.* **24**, 467–478.
- Shibayama, M., Matsunaga, T. & Nagao, M. (2009). *J. Appl. Cryst.* **42**, 621–628.
- Sokolova, A., Christoforidis, J., Eltobaji, A., Barnes, J., Darmann, F., Whitten, A. E. & de Campo, L. (2016). *Neutron News*, **27**(2), 9–13.
- Wagner, V., Friedrich, H. & Wille, P. (1992). *Physica B*, **180–181**, 938–940.
- Well, A. A. van (1992). *Physica B*, **180–181**, 959–961.
- Well, A. A. van & Fredrikze, H. (2005). *Physica B*, **357**, 204–207.
- Wood, K., Mata, J. P., Garvey, C. J., Wu, C.-M., Hamilton, W. A., Abbeywick, P., Bartlett, D., Bartsch, F., Baxter, P., Booth, N., Brown, W., Christoforidis, J., Clowes, D., d’Adam, T., Darmann, F., Deura, M., Harrison, S., Hauser, N., Horton, G., Federici, D., Franceschini, F., Hanson, P., Imamovic, E., Imperia, P., Jones, M., Kennedy, S., Kim, S., Lam, T., Lee, W. T., Lesho, M., Mannicke, D., Noakes, T., Olsen, S. R., Osborn, J. C., Penny, D., Perry, M., Pullen, S. A., Robinson, R. A., Schulz, J. C., Xiong, N. & Gilbert, E. P. (2018). *J. Appl. Cryst.* **51**, 294–314.